Research on Chemical Intermediates (2025) 51:6487–6514
https://doi.org/10.1007/s11164-025-05759-2

Floating Ag-ZnO@PAN nanofiber mats with photocatalytic, piezoelectric, and plasmonic functions for wastewater treatment

Ghazale Asghari Sarabi[1,4] · Morasae Samadi[2] · Habib Bagheri[3] · Md. Golam Kibria[4] · Alireza Z. Moshfegh[1,5]

Received: 9 July 2025 / Accepted: 16 September 2025 / Published online: 7 October 2025

Abstract

Adequate wastewater treatment is crucial for ensuring access to safe and sanitary water, which can be achieved through photocatalytic processes. This work elucidates the preparation of cost-effective and easily scalable polyacrylonitrile (PAN) electrospun nanofibers (NFs) as support for ZnO nanorods (NRs) photocatalysts. Then, Ag nanoparticles (NPs) were homogenously deposited on ZnO NRs/PAN NFs to prepare Ag NPs/ZnO NRs/PAN NFs samples. Photochemical and electrochemical characterization demonstrated a higher photocurrent density and stability for the Ag NPs/ZnO NRs/PAN NFs than ZnO NRs/PAN NFs. In addition, the prepared photocatalysts were utilized for the photodegradation of various dyes, including methylene blue (MB) and rhodamine B (RhB), as well as tetracycline (TC), an antibiotic serving as a model organic pollutant, under different light illumination conditions. The Ag NPs/ZnO NRs/PAN NFs demonstrated 2.4, 2.6, and 1.6 times higher photocatalytic activity than ZnO NRs/PAN for MB, RhB, and TC photodegradation under UV light, respectively. This floating and free-standing mat, with high stability, demonstrated 82% MB removal after 1 h of exposure to outdoor natural light. Mechanistic studies conducted by adding scavengers revealed that generating hot plasmonic electrons on the Ag NPs through illumination plays a pivotal role in improving the photodegradation activity of Ag NPs/ZnO NRs/PAN NFs mats. Furthermore, ultrasonic vibration was also utilized to induce piezoelectricity in the ternary Ag NPs/ZnO NRs/PAN NFs, resulting in an approximately 2.2-fold improvement in the MB photodegradation rate due to the synergistic effects of piezoelectricity and plasmonics. This durable and reusable photocatalyst, with its mechanical robustness and superior self-cleaning characteristics, is a promising system that offers a potential direction for future research and efficient wastewater treatment.

Extended author information available on the last page of the article

Graphical abstract

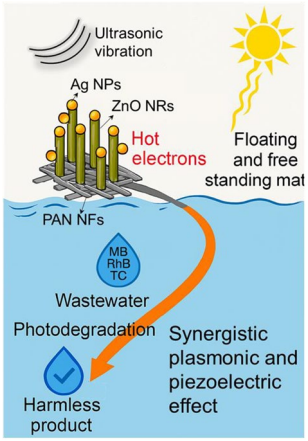

Keywords Elecrospinning · Photodegradation · Emerging pollutants · Organic dyes · Wastewater discharge

Introduction

Emerging pollutants (EPs), including pharmaceutical and personal care products (PPCPs), endocrine-disrupting agents, and synthetic chemicals, are widely discharged into the environment, raising concerns about global public health [1]. According to published reports, synthetic azo dyes and antibiotics are categorized as EPs, and the flow of untreated wastewater containing these organic pollutants into aquatic streams leads to ecosystem disruption and human health threats due to their carcinogenicity risk and persistent nature [2]. Advanced oxidation processes (AOPs) that generate reactive oxygen species (ROS), such as ·OH, H_2O_2, and O_2^-, are potent methods for efficiently removing emerging pollutants [3]. Among AOPs, heterogeneous photocatalysis based on semiconductor nanostructures has garnered considerable attention due to its simplicity and cost-effectiveness. In addition, the complete mineralization of organic pollutants into CO_2 and water by photocatalysts has sparked significant interest in the removal of EPs [4–6].

In the photocatalytic process by a semiconductor, upon light illumination, electrons and holes are generated as charge carriers in the conduction and valence bands, respectively, which migrate to the photocatalyst surface to form ROS as strong oxidants for the degradation and mineralization of organic substances [4, 7]. In recent years, substantial efforts have been devoted to promoting the separation of electron–hole pairs to delay their recombination, a crucial strategy for enhancing photocatalytic activity. Hybridization of the semiconductor-based photocatalyst with other semiconductors and conducting materials such as graphene, carbon nanotubes, and metals has been employed to promote electron–hole separation [8, 9]. Moreover,

recent studies have shown that applying a piezoelectric field to induce polarization within a photocatalyst effectively hinders the recombination of photo-generated charge carriers due to the localized electric field near the photocatalyst surface [10, 11]. The phenomenon of rapid electron–hole recombination in photocatalytic materials can be mitigated by the generation of a space charge field in piezoelectric systems, which accelerates carrier separation and transfer. Consequently, the synergy between the piezoelectric effect and photocatalysis can yield superior photocatalytic performance [12, 13]. Piezo-photocatalytic materials belong to the non-centrosymmetric point groups of crystal structures in which deformation or strain induces polarized negative and positive charges on the two sides and generates an internal electric field, which can hinder the recombination of charge carriers and boost photocatalytic performance [14, 15].

The tetrahedral coordination in ZnO results in alternating Zn^{2+} and O^{2-} planes forming polarization along the c-axis. Therefore, its non-centrosymmetric crystal structure can exhibit piezoelectric properties [16]. Moreover, 1D ZnO NRs with boosted photocatalytic degradation of organic pollutants during light/piezo excitation are promising for effective wastewater treatment containing emerging pollutants [17, 18]. External stress, induced by ultrasonic or mechanical vibrations, can induce piezoelectricity, suppressing electron–hole pair recombination and accelerating the migration of photoexcited carriers due to the formation of a built-in electric field in ZnO nanorods (NRs) [19]. Furthermore, combining ZnO nanostructures with noble metals like Ag and Au, which have surface-polarized electrons, can modify the piezoelectric performance and suppress surface recombination, resulting in enhanced photocatalytic performance towards the degradation of organic pollutants [20–23].

The recovery of the photocatalyst from the treated water is one of the main concerns in the photocatalysis community [24]. Anchoring and immobilizing the photocatalyst material on a flexible polymer nanofiber mat is one of the emerging pathways for fast and straightforward separation to tackle this challenge [25]. Polyacrylonitrile (PAN) is widely recognized as a cost-effective and scalable polymer for the fabrication of nanofibers, with a relatively low raw material cost (approximately \$2–4 per kg) [26]. Its good spinnability and easy modification make PAN suitable for large-scale electrospinning processes [27]. Moreover, PAN-based nanofiber mats exhibit excellent chemical and thermal stability, enabling multiple reuse cycles in various applications, including filtration, catalysis, biomedicine, tissue engineering, and sensing [28, 29]. This study utilized flexible, cost-effective, and scalable polyacrylonitrile (PAN) electrospun mats to grow ZnO nanorods (NRs) photocatalysts. Electrospinning provides a facile and controllable route to produce continuous fibers with tunable diameters from the nanometer to micrometer scale, yielding high porosity, environmentally friendly mats that can serve as effective photocatalyst supports [23, 24, 30, 31]. Nanofibers have a large specific surface area, making them suitable candidates for anchoring photocatalytic nanomaterials [32]. Additionally, ZnO is an abundant, low-cost, and easy-to-obtain metal oxide, making it an ideal candidate for practical photocatalytic applications [33]. This study aims to decorate Ag NPs on ZnO NRs/PAN NFs mats to exploit their surface plasmon resonance and piezo-photocatalytic activity under visible light for the degradation of organic drugs and dyes.

To provide a structured and quantitative overview of the research landscape in piezo-photocatalysis**,** we performed a bibliometric analysis using VOSviewer, focusing on publications from 2015 to June 11, 2025. Co-occurrence of keywords was analyzed to identify major research clusters and emerging trends. Based on the analysis of 678 documents using the Scopus database with a search query string of TITLE("piezo*") AND TITLE("photocatal*"), Fig. 1 demonstrates overlay visualization of the publications. Zinc oxide (ZnO) and barium titanate ($BaTiO_3$)-based piezo-photocatalysts have been reported more frequently, followed by lead titanate ($PbTiO_3$), sodium niobate ($NaNbO_3$), silver niobate ($AgNbO_3$), and strontium titanate ($SrTiO_3$). Recently, the development of carbon-based piezo-photocatalysts by defect and doping engineering of carbon nitride has attracted great interest. Additionally, the synergistic effect of plasmonics and piezoelectrics on the photocatalytic process is an emerging topic that warrants further research and investigation. Density functional theory is another appealing issue to study in depth in the analysis of these types of concepts. This overlay visualization confirms that the field is rapidly expanding toward multi-functional materials, hybrid activation methods, and environmentally relevant contaminants.

Our work focuses on Ag/ZnO nanorods immobilized on PAN nanofibers and activated by ultrasonic waves, aligning with these trends and is an emerging topic that needs further research and investigation. This study introduces a hierarchically engineered ternary composite—Ag NPs/ZnO NRs/PAN NFs—anchored on a flexible, floating nanofibrous mat. The novelty lies in the synergistic integration of plasmonic

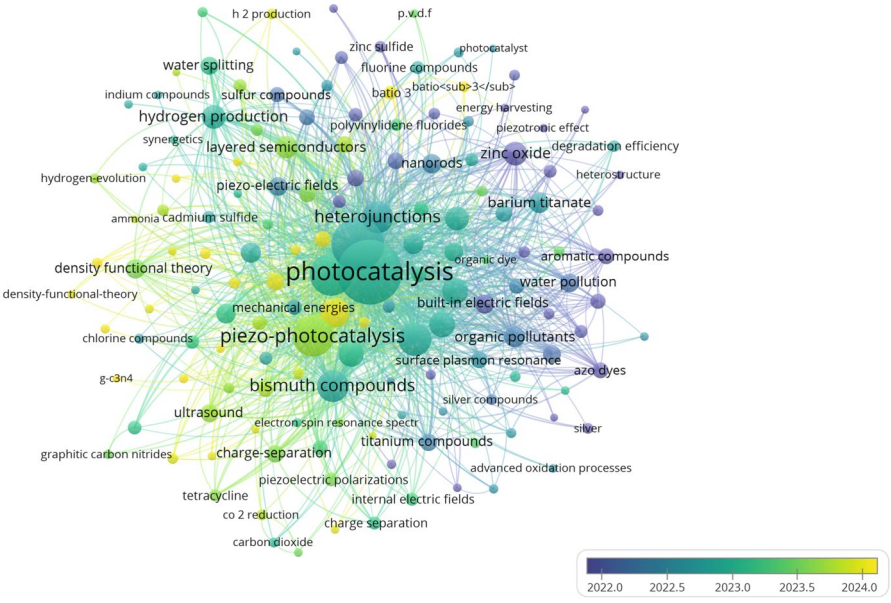

Fig. 1 Overlay visualization of keyword co-occurrence in piezo-photocatalysis research (2022–2024), generated using VOSviewer. Node size represents term frequency; color indicates average publication year (blue = older, yellow = newer).(color figure online)

Ag nanoparticles and piezoelectric ZnO nanorods within a mechanically robust and reusable PAN substrate, enabling enhanced photocatalytic performance under UV, visible, and natural sunlight. Furthermore, the system demonstrates piezo-photocatalytic activity under ultrasonic vibration, a feature rarely reported in similar architectures. Compared to prior works [34–36], our approach offers a multifunctional platform that combines plasmonic enhancement, piezoelectric charge separation, and facile recovery—addressing key challenges in practical wastewater treatment applications.

Materials and methods

Synthesis of ZnO nanorods/PAN nanofibers

A 12 wt% PAN solution in DMF solvent was prepared and then loaded into a 10 mL syringe. The syringe needle was connected to the high-voltage power supply, and the voltage was fixed at 11 kV. A syringe pump controlled the flow rate of the solution, which was set at 1 mL/h, and the distance between the syringe and collector was kept at 10 cm. The fibers were deposited on a rotating drum covered with aluminum foil, and environmental conditions were maintained at 25% humidity and a temperature of 25 °C. The schematic of our setup for electrospinning, along with the applied conditions, is illustrated in Fig. S1. The concentration of PAN in DMF, spinning distance, flow rate, and applied voltage were optimized to fabricate a uniform electrospun mat with an average fiber diameter of approximately 200 nm and a bead-free morphology. In Table S1, various parameters, including applied voltage, spinning distance, flow rate, and polymer concentration, are listed to achieve continuous, smooth, and bead-free fibers.

The prepared PAN NFs mat was used to grow ZnO NRs using the chemical bath deposition (CBD) method. In the first step, a solution containing 5 mM zinc acetate dihydrate ($Zn(CH_3COO)_2{\cdot}H_2O$) and ethanol was prepared as a seed solution. It was stirred for one hour at 60 °C until a transparent solution was obtained. Then, PAN NFs were immersed in the ZnO seed solution using the dip coating method. After drying at room temperature, the dip coating procedure was repeated five times to obtain a sufficient and uniform seed layer thickness. Then, the nanofibers were heated in an oven at 120 °C for two hours to crystallize the ZnO nanoparticles on the substrate. Next, an aqueous solution containing 25 mM zinc nitrate hexahydrate ($Zn(NO_3)_2{\cdot}6H_2O$) and 25 mM hexamethylene tetraamine was prepared as ZnO NRs growth solution. The pre-seeded nanofibrous substrates were suspended in the growth solution at 95 °C on a hot plate stirrer and maintained under stirring for 10 h. Finally, the substrate was rinsed with DI water and dried in air for further use.

Synthesis of Ag nanoparticles/ZnO nanorods/PAN nanofibers

The as-synthesized ZnO NRs/PAN NFs membrane was placed under UV irradiation for 4 h (2 h for each side). Then, a 42 mL solution of 1 wt% $AgNO_3$ in 40 mL water

and 2 mL ethanol was prepared, and the nanofibrous membranes were floated in this solution. Next, the solution was stirred for two hours in the dark. Finally, the nanofibrous membranes were washed three times with deionized (DI) water, dried at 70 °C for 5 h, and used as a photocatalyst. Figure 2 shows the preparation procedure of Ag nanoparticles/ZnO nanorods/PAN nanofibers in a schematic flow chart.

The details of characterizations, photocatalytic activity of MB and TC, and photoelectrochemical measurements are elucidated in the Supplementary material.

Results and discussions

Surface morphology and wettability

To determine the surface morphology and microstructure of the prepared photocatalysts, field emission scanning electron microscopy (FESEM) is utilized. Figure 3a shows the FESEM image of PAN NFs, which are smooth, uniform, and without beads. The inset of this figure shows the photo of PAN NFs, which had a 50 µm average thickness measured by the OSK thickness instrument from 100 different points of nanofibrous layer. The histogram of the nanofiber diameters depicted in Fig. 3b demonstrates uniform diameter distribution with an average diameter of about 211 ± 5 nm (evaluated by Image J software, 100 points). The cross-section morphology of PAN NFs was obtained by floating them into epoxy resin (Fig. 3c). The circular cross-section is observable, and the diameter size of the nanofibers was consistent with the results obtained from surface imaging analysis. Figure 3d represents FESEM images of ZnO NRs on the surface of PAN NFs with an average length and diameter of ~ 1.2 µm and 170 nm, respectively. In Fig. 3e, the deposition of Ag NPs on ZnO NRs is evident, with an average diameter of approximately 46 ± 18 nm. The corresponding EDX mapping images in Fig. 3f–h show a uniform distribution of Zn, O, and Ag elements over the surface of the ZnO NRs.

The contact angle studies were performed for the Ag NPs/ZnO NRs/PAN NFs, ZnO NRs/PAN NFs, and PAN NFs layers, which showed their hydrophilic nature (Fig. S2).

The initial water contact angles measured at 1*s* for PAN NFs, ZnO NRs/PAN NFs, and Ag NPs/ZnO NRs/PAN NFs were 47°, 81°, and 85°, respectively, indicating a progressive decrease in hydrophobicity with surface modification. The presence of vertically aligned ZnO nanorods and surface-decorated Ag nanoparticles, as confirmed by FESEM images, significantly alters the surface morphology of

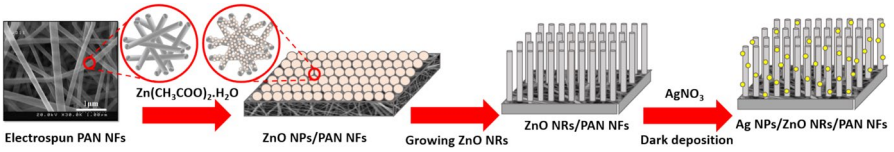

Fig. 2 Flow chart of the experimental fabrication process of ZnO NRs, Ag NPs, and overall Ag NPs/ZnO NRs/PAN NFs

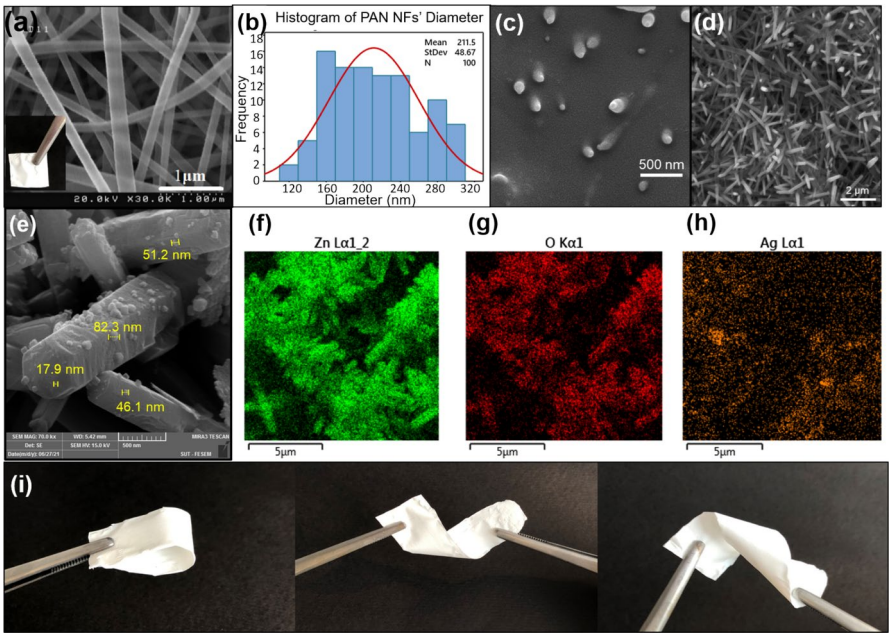

Fig. 3 **a** FESEM images of PAN nanofibers, **b** PAN nanofibers diameter distribution, FESEM images of **c** the cross-section of PAN NFs, **d** ZnO NRs/ PAN NFs, and **e** Ag NPs/ ZnO NRs/ PAN NFs, **f–h** elemental map of Ag NPs/ZnO NRs/PAN NFs, and **i** Photographs of flexibility, bendability, and twist ability of the ZnO NRs/PAN NFs

the PAN nanofibrous mats. These hierarchical nanostructures increase the surface roughness, causing water droplets to rest atop the protruding features while trapping air pockets within the valleys of the fibrous network. This configuration initially enhances apparent hydrophobicity, as observed in similar systems such as h-PVDF-Ag, where nanostructure-induced roughness led to contact angles exceeding 110° [37]].

However, the water contact angles decreased significantly after 10 and 50 s, reflecting rapid water absorption and confirming the underlying hydrophilic nature of the nanofibrous mats. Rapid lateral spreading of water across the nanofiber network, allowing it to penetrate the porous structure of the mat as reprted by other reserchер[38]. This behavior suggests that while surface roughness and nanoparticle loading initially decrease apparent hydrophobicity, the porous structure and polar functional groups facilitate water penetration over time. This fast absorption is beneficial for photocatalytic applications, as it enhances pollutant–catalyst contact and accelerates reaction kinetics in aqueous environments.

Mechanical and thermal characterization

It is well established that the mechanical properties of photocatalysts, particularly robustness and stability, are key issues in long-term reaction processes for industrial

applications. These unique properties make them promising photocatalysts for efficient wastewater treatment through direct extraction, eliminating the need for post-processing. The PAN NFs layer and ZnO NRs/PAN NFs also exhibited excellent mechanical flexibility (see SI movies). Both fibrous membranes could be bent to 180° and back to their original state without any visible structural damage or loss of the ZnO NRs from the nanofibrous substrate (Fig. 3i) These membranes can be folded, rolled, curled, and twisted into various shapes without compromising their original appearance (see the video file in the SI file). As a result, these nanofibrous membranes have good flexibility and self-supporting properties, which are essential properties for practical photocatalytic applications.

To verify the mechanical properties, tensile testing was also carried out for the Ag NPs/ZnO NRs/PAN NFs, ZnO NRs/PAN NFs, and PAN NFs; the stress–strain curves of these fibrous mats are illustrated in Fig. S3. PAN NFs possessed an elastic modulus of 190.6 MPa and ultimate tensile strength (σ_{UTS}) of 8.6 MPa. After depositing ZnO NRs on the PAN NFs, the elastic modulus and σ_{UTS} increased to 224.7 MPa and 14.5 MPa, respectively. Similarly, after depositing Ag NPs on the ZnO NRs/PAN NFs mats, the elastic modulus and σ_{UTS} increased to 350.3 MPa and 16.3 MPa, respectively. From Young's elastic modulus value, which reflects the material's stiffness, the above results imply that depositing ZnO NRs and Ag NPs can enhance the mechanical properties of PAN NFs, making them useful for practical photocatalytic applications.

The mechanical properties of nanofibrous membranes can be significantly improved through surface modification with inorganic nanostructures [38]. Growing ZnO nanorods and Ag nanoparticles restricts polymer chain mobility, resulting in increased stiffness and tensile strength [38]. These nanostructures act as mechanical reinforcements, distributing applied stress more efficiently across the fiber matrix. A similar improvement has been reported in electrospun systems, where hierarchical surface architectures contribute to both mechanical robustness and operational durability under repeated deformation [39].

Thermogravimetric analysis and the weight loss pattern of the PAN NFs, ZnO NRs/PAN NFs, and Ag NPs/ZnO Ns/PAN NFs as a function of heating temperature in an air atmosphere are shown in Fig. S4. In PAN NFs, the observed weight reduction below 300 °C is attributed to the loss of moisture from physisorbed water and its subsequent evaporation [40]. PAN polymer is stable up to 300 °C; however, above this temperature, side chain degradation and decomposition of the carbon–carbon main chain occur, as previously reported [41]. Compared to PAN NFs, the thermal degradation curves of the ZnO NRs/PAN NFs and Ag NPs/ZnO NRs/PAN NFs shift to a high-temperature region, which confirms that the thermal stability of PAN NFs is greatly enhanced after the growth of ZnO NRs and Ag NPs. This can be related to the adhesion between polymers and inorganic surfaces, as well as the heat shielding effect [42]. Weight residues of the ZnO NRs/PAN NFs and Ag NPs/ZnO NRs/PAN NFs are more than those of PAN NFs since ZnO NRs and Ag NPs are thermally stable below 1000 °C. Hence, the increase in the weight residue of the nanofibrous membrane is due to the presence of ZnO NRs and Ag NPs. By analyzing TGA curves in an air atmosphere, the mass difference between the PAN NFs and ZnO NRs/PAN NFs curves at 1000 °C shows 19.3 wt% residues, which can

be attributed to the presence of ZnO NRs. Moreover, the mass difference between Ag NPs/ZnO NRs/PAN NFs and ZnO NRs/PAN NFs curves is 11.9 wt%, demonstrating the amount of Ag NPs loaded on ZnO NRs.

Thermogravimetric analysis (TGA) revealed that the residual weight of ZnO NRs/PAN NFs and Ag NPs/ZnO NRs/PAN NFs was significantly higher than that of pristine PAN NFs, indicating enhanced thermal stability due to the presence of inorganic nanostructures. It is important to note that ZnO remains thermally stable within the decomposition range of the polymer matrix (up to ~ 600 °C), which is an appropriate temperature window for our measurements. The increased char residue is attributed to the non-volatile nature of ZnO and Ag phases under these conditions.

Crystal structure, chemical bonding, and physical properties

The crystalline nature of the catalysts was examined with the XRD pattern, as shown in Fig. 4a. The XRD pattern of pristine PAN nanofibers exhibits a distinct diffraction peak at $2\theta = 17.3°$, corresponding to the orthorhombic lattice reflection characteristic of PAN. Upon growth of ZnO nanorods, the composite ZnO NRs/PAN NFs displays sharp peaks matching the hexagonal wurtzite structure of ZnO (PDF NO. 98-100-1316), confirming successful crystallization. For the Ag NPs/ZnO NRs/PAN NFs sample, no additional peaks attributable to Ag were observed, likely due to the low Ag loading, which falls below the detection threshold of the diffractometer. As a result, the XRD pattern closely resembles that of ZnO NRs/PAN NFs. These data collectively confirm the structural integrity and phase composition of the fabricated nanofibrous systems. The peaks matched ZnO's typical hexagonal wurtzite structure (PDF No. 98-100-1316) as reported recently [43]. The lattice parameters are $a = b = 0.324$ nm and $c = 0.519$ nm, with $c/a = 1.6019$, which agrees with the standard card. It is worth noting that a similar XRD pattern is also observed for the Ag NPs/ZnO NRs/PAN NFs, and no peaks belonging to other phases were observed due to the low concentration of silver in the sample.

XPS is a very sensitive technique for investigating surface chemical compositions of solid materials. The XPS survey spectrum of the Ag NPs/ZnO NRs/PAN NFs is shown in Fig. S5, confirming the presence of Ag, Zn, O, C, and N elements. In the deconvoluted Zn 2*p* spectrum shown in Fig. 4b, the Zn element has a higher intensity for the Zn $2p_{3/2}$ with a binding energy centered at 1021.5 eV and a lower intensity observed for the Zn $2p_{1/2}$ with a binding energy centered at 1044.7 eV. These results confirmed that the zinc on the surface is present in the form of Zn^{2+} within the ZnO structure [44]. Figure 4c illustrates the deconvoluted Ag 3*d* spectrum, which consists of two separate peaks: Ag $3d_{5/2}$ and Ag $3d_{3/2}$, with binding energies centered at 367.9 eV and 373.8 eV, respectively. This indicates that the silver in the Ag NPs/ZnO NRs/PAN NFs sample mainly presents as an Ag metallic form in the zero-valent state [21]. Therefore, in our work, the dark deposition synthesis of Ag facilitated the growth of Ag^0 NPs and inhibited the formation of Ag_2O, as reported by others [45]. Moreover, the binding energy of the Ag 3*d* core level spectrum slightly shifts compared with the Ag bulk binding energy (368.2 eV and 374.2 eV). This shift can be due to the electron transfer from Ag to ZnO, which decreases the

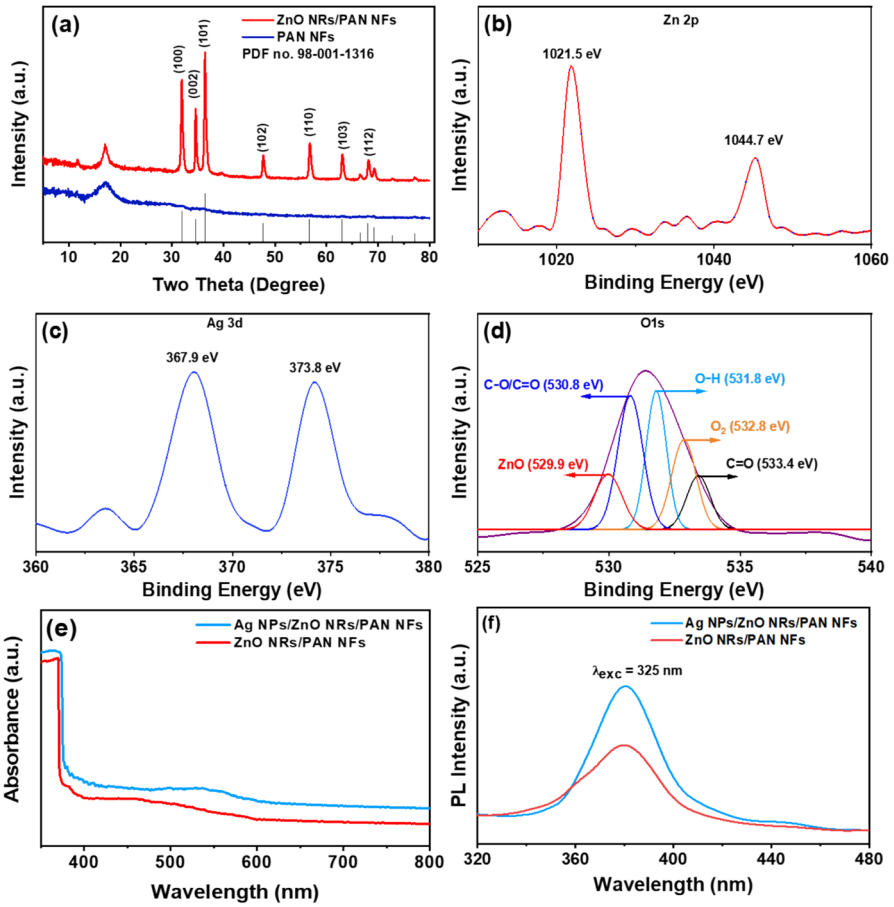

Fig. 4 **a** XRD pattern of ZnO NRs/PAN NFs and PAN NFs. **b** high-resolution XPS spectrum of the Zn 2*p*, **c** high-resolution XPS spectrum of the Ag 3*d*, and **d** the deconvoluted O 1*s* spectrum, **e** UV–visible absorption spectra of the Ag NPs/ZnO NRs/PAN NFs and ZnO NRs/PAN NFs, and **f** Photoluminescence measurements for the ZnO NRs/PAN NFs and Ag NPs/ZnO NRs/PAN NFs photocatalysts

binding energy of Ag, as reported by other studies [45, 46]. Figure 4d shows the O 1*s* core-level spectrum, which can be deconvoluted into five peaks. The peak centered at a binding energy of 529.9 eV is associated with O^{2-} ions in the hexagonal wurtzite structure of ZnO, as measured and reported by others [44, 47]. The second peak, with a binding energy of 530.8 eV, is related to the C=O bond, which is generally associated with oxygen vacancies [48]. The third and fourth peaks at 531.8 and 532.8 eV correspond to the adsorption of hydroxyl ions (OH^-) and oxygen molecules (O_2) on the surface, respectively [47, 49]. Finally, the fifth peak at around 533.4 eV is assigned to O–C=O [48].

Figure S6a demonstrates the N_2 adsorption–desorption isotherms for different materials, and specific surface areas were calculated. According to the IUPAC

classification, the obtained isotherms are typical type *V* with an H3 hysteresis loop, indicating the mesoporous nature of the samples. Figure S6b shows the pore-size distribution of the sample estimated using the Barrett-Joyner-Halenda (BJH) method. Table S2 summarizes the observed surface area and pore size of the samples. The growth of the ZnO NRs decreases the specific surface area of the PAN NFs, and the deposition of Ag NPs leads to an increase in surface area. The higher specific surface area played a key role in photocatalytic activity due to the presence of more accessible active sites for the adsorption of pollutants and the decontamination process over the photocatalysts. A similar enhancement in surface area and porosity upon incorporation of ZnO and Ag species into PVDF electrospun nanofibers has been reported previously [50].

Optical property

Optical absorbance spectroscopy was employed to examine the optical characteristics of the Ag NPs/ZnO NRs/PAN NFs and ZnO NRs/PAN NFs, as illustrated in Fig. 4e. The peak absorbance is observed at approximately 372 nm, attributed to ZnO's inherent wide bandgap properties [51]. The deposition of noble metals, such as Ag, on the surface of ZnO nanorods (NRs) can enhance the absorbance intensity across all wavelengths. The most significant increase in absorbance intensity occurs around 550 nm, which may be attributed to the localized surface plasmon resonance (SPR) effect associated with the Ag NPs. Increasing visible light absorption by adding Ag to the ZnO sample has been reported in other published studies [34, 52, 53].

The UV–visible diffuse reflectance spectra of the Ag NPs/ZnO NRs/PAN NFs and ZnO NRs/PAN NFs are shown in Fig. S7a. The reflectance intensity (%*R*) in the visible light region decreased sharply in the Ag NPs/ZnO NRs/PAN NFs compared with ZnO NRs/PAN NFs. This is likely due to light absorption resulting from the surface plasmon resonances (SPRs) of the Ag NPs, leading to a decrease in reflectance. Therefore, there is a coupling between the Ag NPs' SPRs and ZnO NRs, as reported by others [54].

The reflectance intensity (%*R*) was used to calculate the band gap energy (E_g) by using the following Kubelka–Munk equation [6]:

$$F(R) = \frac{(1-R)^2}{2R} \tag{1}$$

The graph of $(F(R)\mathrm{h}\nu)^2$ as a function of $\mathrm{h}\nu$ is plotted in Fig. S7b, and the resulting intercept represents the band gap energy of the corresponding photocatalyst. The band gap energies of the materials, obtained through the extrapolation of the linear portion of the Kubelka–Munk graph for direct band gap semiconductors of ZnO NRs and Ag NPs/ZnO NRs, are estimated to be approximately 3.35 eV and 3.21 eV, respectively.

Figure 4f shows the PL emission spectra of the ZnO NRs/PAN NFs and Ag NPs/ZnO NRs/PAN NFs. A near-band-edge emission centered at 380 nm (~3.26 eV) in the UV region is located near the band edge of ZnO. Based on Fig. 4f, the intensity of this PL peak increases upon the decoration of Ag NPs on the ZnO NRs/PAN NFs.

Singh et al. reported a similar result in the Ag-TiO_2 sample, correlating the increasing PL intensity with the injection of Ag-hot plasmonic electrons into the TiO_2 conduction band [55]. They concluded that these electrons significantly enhanced the electron density in TiO_2 and magnified the emitted photons from the sample. Therefore, this concept agrees with our DRS data analysis and is validated by the PL results. This finding is consistent with other studies that have shown an increase in PL intensity related to the SPR effect of Ag NPs [56–58].

Photochemical and electrochemical characterization

Figure S8a presents LSV (J–V) results of the samples under both dark and light illumination conditions. As anticipated, PAN NFs showed no current density in the dark or under light irradiation. Under dark condition, the current densities at 0.5 V bias voltage for the Ag NPs/ZnO NRs/PAN NFs and ZnO NRs/PAN NFs were measured at about 11 and 9 μA/cm^2, respectively. Under light irradiation, the photocurrent densities of the Ag NPs/ZnO NRs/PAN NFs and ZnO NRs/PAN NFs were increased to 22 and 17 μA/cm^2, respectively (Fig. S8b).

The chronoamperometry analyses for the Ag NPs/ZnO NRs/PAN NFs, ZnO NRs/PAN NFs, and PAN NFs were examined, and the results are depicted in Fig. 5a with 0.5 V versus RHE for 390 s. As expected, PAN NFs have no photocurrent output. The photocurrent densities of the Ag NPs/ZnO NRs/PAN NFs and ZnO NRs/PAN NFs after 390 s were around 19.44 and 14.68 μA/cm^2, respectively. Therefore, we observed higher photocurrent density and stability for Ag NPs/ZnO NRs/PAN NFs than ZnO NRs/PAN NFs. In addition, both samples exhibited a fast photoresponse due to the greater number of photo-generated electrons that transfer from the Ag NPs/ZnO NRs/PAN NFs to the counter electrode via the external circuit. Upon turning on illumination, photocurrent density increases rapidly and reaches a stable value. The resulting photocurrent response demonstrates that the change in photocurrent density is related to the photosensitivity of the working electrode under light-on and off-chopping conditions, indicating that the photo-generated charge transfer is a rapid process [59].

The photo-generated charge transfer process at the semiconductor–electrolyte interface is further investigated by photoelectrochemical impedance spectroscopy (PEIS) [60]. Nyquist plots of ZnO NRs/PAN NFs and Ag NPs/ZnO NRs/PAN NFs electrodes are shown in Fig. 5b. It is observed that the radius of the arc on the PEIS Nyquist plot of the Ag NPs/ZnO NRs/PAN NFs is smaller than that of the ZnO NRs/PAN NFs under simulated sunlight irradiation, indicating a decrease in charge transfer resistance after the deposition of Ag NPs and reducing the accumulation of the charge density at the surface of ZnO. The electron-transfer resistance (R_{ct}) values can be analyzed in the high-frequency region of the Nyquist plots in PEIS measurements and are equivalent to the diameter of the semicircle. Under light illumination, the order of R_{ct} values is as ZnO NRs/PAN NFs > Ag NPs/ZnO NRs/PAN NFs, which can prove that the deposition of Ag NPs can reduce the charge transfer resistance of photo-generated carriers and consequently accelerate the interfacial charge transfer. Moreover, as shown in Fig. 5c, the stability of the current density

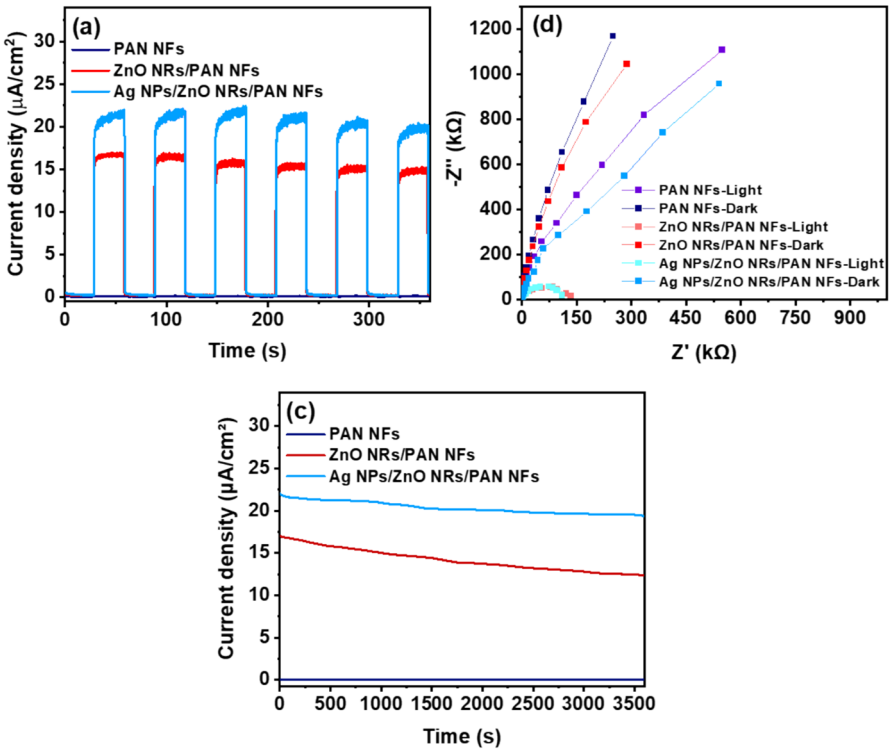

Fig. 5 **a** Photocurrent response curves under chopped light collected, **b** Nyquist impedance diagram, and **c** chronoamperometry analysis. Photoreduction-processed for the PAN NFs, ZnO NRs/PAN NFs, and Ag NPs/ZnO NRs/PAN NFs in 0.5 M Na_2SO_4 solution under simulated sunlight irradiation with the intensity of 100 mW/cm^2 and the scan rate of 50 mV/s

of the Ag NPs/ZnO NRs/PAN NFs is greater than that of ZnO NRs/PAN NFs after 3600 s. In the presence of simulated sunlight irradiation in a 0.5 M Na_2SO_4 solution, the current density of the Ag NPs/ZnO NRs/PAN NFs and ZnO NRs/PAN NFs retained about 87.8% and 72.7% of their quantity at the starting point after 3600 s, respectively. The effective photoelectronic conversion properties are attributed to the simultaneous promotion of light harvesting and the separation of photo-generated charge carriers in the Ag NPs/ZnO NRs/PAN NFs. These processes are essential steps toward enhanced photocatalytic and photoelectrochemical reactions.

Photocatalytic activity measurements

Photocatalytic activity under UV light irradiation

To investigate and compare the photocatalytic performance of all prepared samples, MB, RhB, and TC, which serve as models for organic pollutants, were used to assess their photodegradation activity. The variation in MB and RhB concentration was

monitored by changes in the related absorption spectrum at $\lambda_{max} = 664$ and 553 nm. Kinetic studies have demonstrated that the photocatalytic reaction obeys the Langmuir–Hinshelwood apparent first-order kinetics model, which can be simplified to the following equation at low initial concentrations (C_0) of the pollutants [16]:

$$\ln\left(\frac{C_0}{C}\right) = k_{app^*}t \tag{2}$$

where C_0 and C are pollutant concentrations at the initial and final times t. The quantity k_{app} is the apparent first-order rate constant and can be determined as the slope of the graph of $\ln(C_0/C)$ versus reaction time t under light irradiation. Figure 6a shows the photocatalytic activity of the samples for MB degradation. Before any photocatalytic experiment, the self-standing membrane was immersed in MB solution with a concentration of 10 μM and stirred slightly in the dark for 60 min to achieve adsorption–desorption equilibrium between MB and the photocatalyst surface. The photodecomposition of MB was not apparent in the absence of the photocatalyst, indicating that the photolysis process was not significant; hence, it confirms the reliability of the photocatalytic characteristic of the sample. The pure PAN NFs exhibit weak photocatalytic activity, which is related to the adsorption of the MB dye solution. However, the ZnO NRs/PAN NFs and the Ag NPs/ZnO NRs/PAN NFs membranes exhibit high photocatalytic performance.

The degradation efficiency of MB over each photocatalyst under UV irradiation was calculated using the following equation [6]:

$$\text{Photodegradation Efficiency}(\%) = \frac{(C - C_0)}{C_0} \times 100 \tag{3}$$

The photodegradation efficiencies of MB reached $89.9 \pm 1.5\%$ in 240 min and $98.8 \pm 0.5\%$ in 180 min for the ZnO NRs/PAN NFs and Ag NPs/ZnO NRs/PAN NFs, respectively. The Ag NPs/ZnO NRs/PAN NFs showed a related rate constant about 2.4 times higher than that of the ZnO NRs/PAN NFs. The results affirm that the photocatalytic properties of the ZnO NRs/PAN NFs membranes were remarkably increased by Ag decoration and synergistic coupling between Ag NPs and ZnO NRs.

The photocatalytic activity of the samples for RhB was conducted under UV light irradiation with the same method as MB photodegradation (Fig. 6b). The photolysis rate and the rate of photodegradation by the PAN NFs are not significant. However, the ZnO NRs/PAN NFs and the Ag NPs/ZnO NRs/PAN NFs membranes demonstrated high photocatalytic activity. The Ag NPs/ZnO NRs/PAN NFs showed the highest photocatalytic activity with a related rate constant of about 2.6 times higher than that of the ZnO NRs/PAN NFs. Furthermore, the photodegradation efficiencies of RhB reach $61.6 \pm 1.5\%$ in 240 min and $34.9 \pm 0.8\%$ in 240 min for the ZnO NRs/PAN NFs and Ag NPs/ZnO NRs/PAN NFs, respectively. Similar to MB photodegradation, the results prove that the photocatalytic properties of the ZnO NRs/PAN NFs membranes were significantly enhanced by Ag decoration and synergistic coupling between Ag NPs and ZnO NRs components.

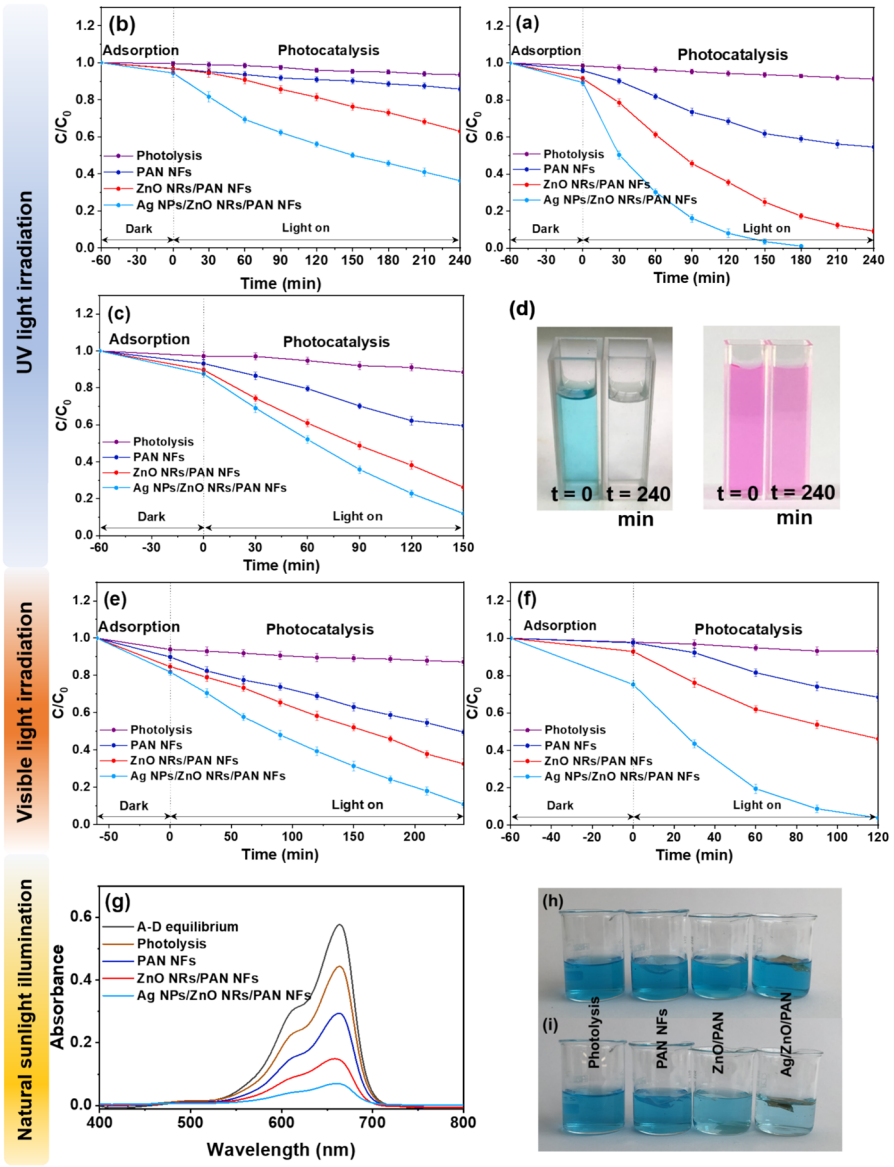

Fig. 6 The change in concentration (C/C_0) versus time for photodegradation of **a** MB, **b** RhB and **c** TC by different samples under UV light irradiation, **d** visual comparison of MB and RhB degradation over time, the change in concentration (C/C_0) versus time for photodegradation of MB **e** under visible white LED and **f** solar simulator irradiation, **g** absorption spectra of MB solution over different samples after 1 h natural sunlight illumination. The related photograph of the MB solution was exposed to different samples after the adsorption–desorption (A–D) equilibrium **h** and after one hour under outdoor sunlight photoirradiation (i)

The photocatalytic decomposition of TC was also studied by recording the changes in its absorption peaks at $\lambda_{max} = 361$ nm in the UV–Vis absorption spectrum. As shown in Fig. 6c, with increasing UV irradiation time, the intensity of the absorption peak over the Ag NPs/ZnO NRs/PAN NFs decreases faster than that of the ZnO NRs/PAN NFs, indicating the excellent photodecomposition ability of the Ag NPs decorated on ZnO NRs. It should be noted that the photolysis rate is insignificant, and the photodegradation activity of the PAN NFs shows a lower rate than that of others. Moreover, according to Fig. 6c, the rate constants of Ag NPs/ZnO NRs/PAN NFs and ZnO NRs/PAN NFs were approximately $1.2 \pm 0.7 \times 10^{-2}$ and $7.5 \pm 0.2 \times 10^{-3}$ min^{-1}, respectively. The Ag NPs/ZnO NRs/PAN NFs exhibited the highest photocatalytic activity, and its rate constant is about 1.6 times higher than that of the ZnO NRs/PAN NFs catalyst for tetracycline degradation.

Photocatalytic performance under LED and solar simulator irradiation

The photodegradation of MB over photocatalysts was achieved using a homemade LED reactor, which consisted of 8 visible white LEDs (Fig. S9). Photocatalytic activity of the samples for the decomposition of MB under LEDs and simulated sunlight illumination is shown in Fig. 6e, f. As can be seen, the rates of MB photolysis and degradation by PAN NFs are very low in both cases. Based on our experimental results, photodegradation of MB over the Ag NPs/ ZnO NRs/PAN NFs and ZnO NRs/PAN NFs was $86.7 \pm 1.9\%$ and $61.6 \pm 2.1\%$ after 240 min under white LEDs irradiation, respectively. The Ag NPs/ZnO NRs/PAN NFs sample demonstrated the highest photocatalytic activity ($k = 7.2 \pm 0.04 \times 10^{-2}$ min^{-1}) compared to the ZnO NRs/PAN NFs ($k = 3.6 \pm 0.01 \times 10^{-2}$ min^{-1}). The apparent rate constant of the Ag NPs/ZnO NRs/PAN NFs sample is approximately twice that of the ZnO NRs/PAN NFs.

Moreover, photodegradation of MB over the Ag NPs/ ZnO NRs/PAN NFs under solar simulator irradiation was measured at about $95 \pm 2.7\%$ after 120 min (Fig. 6f). However, the photodegradation efficiency over ZnO NRs/PAN NFs was $50.4 \pm 1.3\%$ under similar conditions. It was found that the Ag NPs/ZnO NRs/PAN NFs exhibited the highest photocatalytic activity ($k = 2.4 \pm 0.03 \times 10^{-2}$ min^{-1}) as compared to the ZnO NRs/PAN NFs sample ($k = 6.1 \pm 0.02 \times 10^{-3}$ min^{-1}). The measured apparent rate constant of the Ag NPs/ZnO NRs/PAN NFs is around 4 times higher than that of ZnO NRs/PAN NFs. These results proved that the synergistic effect of Ag NPs deposited on ZnO NRs enhances the photodegradation reaction.

Photocatalytic performance under natural outdoor solar light

One of the main goals of the photocatalytic process is the degradation of organic pollutants under natural sunlight illumination for practical applications. To test the ability of MB photodegradation under outdoor sunlight exposure, a beaker containing 20 mL of MB for different photocatalysts was exposed to natural outdoor sunlight from 12:00 to 1:00 PM on June 15, 2024, at the Sharif University of Technology in Tehran. After the adsorption–desorption equilibrium process, the Ag NPs/ ZnO NRs/PAN NFs and ZnO NRs/PAN NFs can degrade MB to $82.2 \pm 4.5\%$ and

62.6 ± 3.6% in 60 min, respectively (Fig. 6g). The apparent change in the color of MB dye after 60 min exposure to outdoor sunlight is shown in Fig. 6h, i. Moreover, the floating photocatalyst structures are apparent in the images. This result demonstrates that the prepared photocatalysts possess high potential activity for practical applications, which can be utilized for the photodegradation of organic compounds in chemical industries.

Photocatalytic reaction mechanism

The photodegradation mechanisms of the MB dye over the photocatalysts were systematically evaluated by trapping the reactive oxygen species (ROS) using different scavengers, including t-butyl alcohol (t-BuOH, 10 mM), ethylenediaminetetraacetic acid disodium salt (EDTA-2Na, 10 mM), $AgNO_3$ (10 mM) as effective ·OH, hole and electron scavengers, respectively [21]. Furthermore, oxygen was added to the dye solution by bubbling the O_2 gas for $\cdot O_2^-$ formation. As illustrated in Fig. 7a, for the MB photodegradation of the ZnO NRs/PAN NFs in the presence of different scavengers, the k value did not change dramatically in the presence of $AgNO_3$ and under O_2 bubbling conditions. Hence, it can be realized that e^- could not play an influential role in the photocatalytic degradation of MB over the ZnO NRs/PAN NFs. However, adding t-BuOH as ·OH scavenger decreases the *k* value from $8.8 \pm 0.4 \times 10^{-3}$ to $4.1 \pm 0.2 \times 10^{-3}$ min^{-1}, which confirms ·OH effectively influences the photocatalytic activity. Moreover, decreasing the *k* value to $1.6 \pm 0.3 \times 10^{-3}$ min^{-1} in the presence of EDTA as an h^+ scavenger shows that the holes were the main reactive oxidation species in the degradation process.

Different scavengers were also added to understand the reaction mechanism further and determine the photocatalytic activity pathway for the Ag NPs/ZnO NRs/PAN NFs. The results are illustrated in Fig. 7b. In the presence of $AgNO_3$, the k

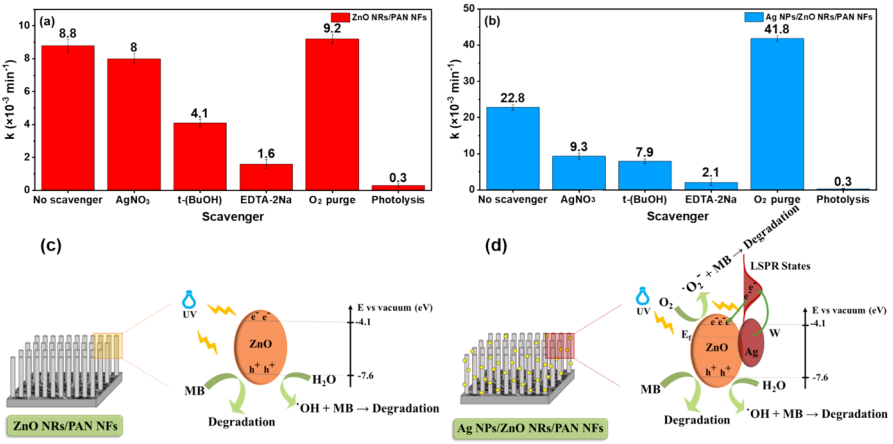

Fig. 7 Measured apparent rate constants in the presence of different scavengers for MB degradation over **a** ZnO NRs/PAN NFs and **b** Ag NPs/ZnO NRs/PAN NFs, Proposed charge transfer mechanisms in photocatalytic degradation of MB over **c** ZnO NRs/PAN NFs and **d** Ag NPs/ZnO NRs/PAN NFs

value of MB photodegradation reduces from $22.8 \pm 0.8 \times 10^{-3}$ to $9.3 \pm 0.8 \times 10^{-3}$ min^{-1}. It indicates that e^- could play an essential role in photocatalytic degradation over the Ag NPs/ZnO NRs/PAN NFs sample. Furthermore, the result of O_2 bubbling shows a remarkable increase in the k value. Therefore, e^- and $\cdot O_2^-$ are mainly effective in the photodegradation process. In addition, by adding t-BuOH and EDTA, the k values decrease to $7.9 \pm 0.6 \times 10^{-3}$ and $2.1 \pm 0.9 \times 10^{-3}$ min^{-1}, respectively. These results show that ·OH and h^+ species play an essential role during MB photodegradation reaction pathways.

Based on the above discussion, we can conclude that ·OH and h^+ were vital reactive species over the ZnO NRs/PAN NFs, and e^-, $\cdot O_2^-$, ·OH and h^+ were effective reactive species over the Ag NPs/ZnO NRs/PAN NFs photocatalysts during MB photocatalytic degradation under UV irradiation. Therefore, according to the obtained results, the proposed MB degradation mechanism is depicted in Fig. 7c, d for the ZnO NRs/PAN NFs and Ag NPs/ZnO NRs/PAN NFs, respectively. The *k* values of photodegradation in the ZnO NRs/PAN NFs demonstrated that ·OH and h^+ are the main species for photocatalytic degradation. Therefore, the photo-generated holes in the ZnO valence band (VB) can directly contribute to the photodegradation process. Additionally, the reaction between water and holes generates ·OH, which assists in MB degradation. In the Ag NPs/ZnO NRs/PAN NFs photocatalyst, in addition to ·OH and h^+, it was found that e^- and $\cdot O_2^-$ species have a decisive role in the photodegradation process. Therefore, upon UV irradiation, hot electrons are generated in Ag metallic particles due to the excitation of localized surface plasmon resonances, and they transfer to the ZnO conduction band (CB), which was confirmed by our DRS and PL results. Consequently, the enhanced photocatalytic activity of the Ag NPs/ZnO NRs/PAN NFs was due to the synergistic effect between Ag NPs and ZnO NRs, due to the injection of hot plasmonic electrons from Ag NPs to the conduction band of the ZnO NRs, as depicted in Fig. 7d.

Although ESR analysis was not performed in this study, previous reports have successfully employed ESR and complementary techniques to confirm the generation of reactive oxygen species in similar photocatalytic systems. These studies provide valuable mechanistic insights into the active roles of ·OH and $\cdot O_2^-$ radicals in pollutant degradation and can serve as a reference framework for interpreting our scavenger-based findings [61–67].

Recyclability, stability, and self-cleaning test

The recyclability and stability of the photocatalysts during successive usages play a vital role in the industrial aspect of practical applications. As mentioned in the previous section, nanofibrous membranes exhibit excellent flexibility, foldability, bendability, twistability, and self-supporting structural behavior. These layers float on the aqueous solution during the photocatalytic degradation process. Fig. S10 displays excellent structural integrity and self-supporting performance after photocatalytic degradation of methylene blue. Therefore, our photocatalyst membrane can be easily removed from the dye solution using tweezers without requiring any long-term processes, such as precipitation, filtration, or centrifugation.

To monitor the stability of our photocatalysts during successive usage, the decomposition efficiencies of MB using ZnO NRs/PAN NFs and Ag NPs/ZnO NRs/PAN NFs were investigated during five cycles of the photocatalytic process. As illustrated in Fig. 8a, the efficiency slightly reduces from 89.9% to 84.6% after five different runs over the ZnO NRs/PAN NFs. The results suggested that the ZnO NRs/PAN NFs photocatalyst membrane maintains a high photocatalytic activity for MB degradation under UV light irradiation. In addition, the XRD pattern of the ZnO NRs/PAN NFs membrane was studied after five sequential cycles to investigate its long-term stability and anti-photo-corrosion properties. As depicted in Fig. S11, no structural changes or other diffraction peaks were

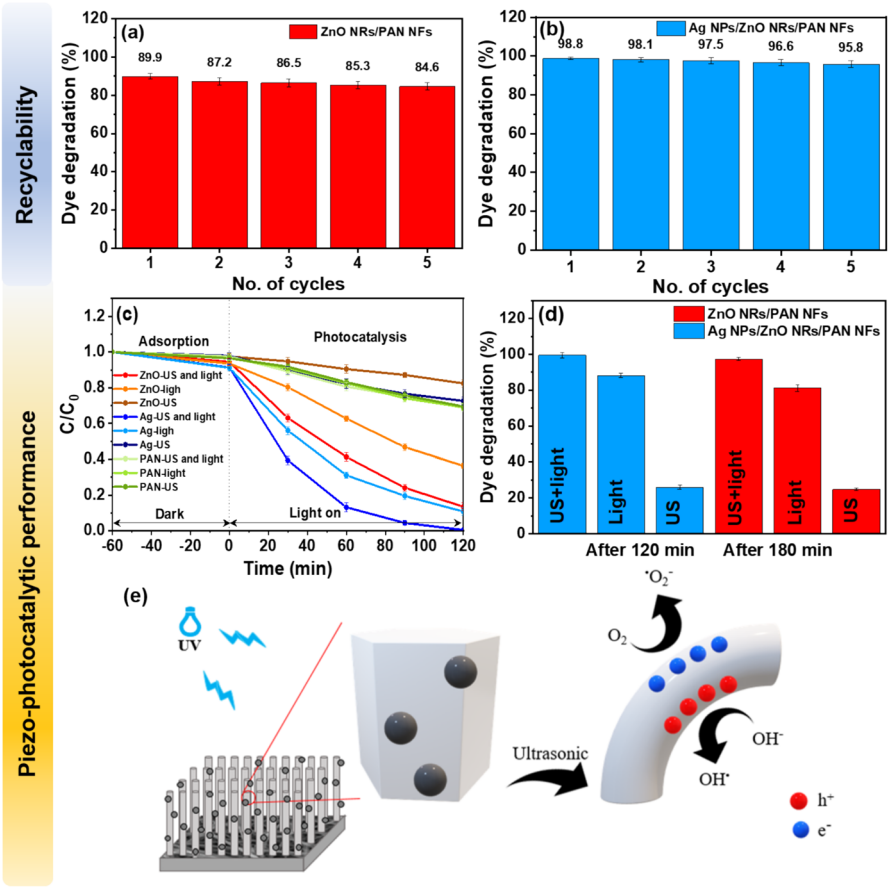

Fig. 8 MB photodegradation of the **a** ZnO NRs/PAN NFs and **b** Ag NPs/ZnO NRs/PAN NFs for five sequential cycles under UV light irradiation, **c** The change in concentration C/C_0 versus time for MB photodegradation using different photocatalysts under ultrasonic (US), light, and both of them (US + light). **d** Measured apparent rate constants after 120 and 180 min for MB degradation over the Ag NPs/ZnO NRs/PAN NFs and ZnO NRs/PAN NFs photocatalysts, and **e** Possible pathway for piezo-photocatalysis and ROS generation

observed after five cycles of the photocatalytic process, confirming its good chemical stability.

In addition, the Ag NPs/ZnO NRs/PAN NFs photocatalyst shows a photodegradation reduction rate from 98.8% to 95.8% after five different cycles, as shown in Fig. 8b. Therefore, the samples exhibit good photostability under prolonged UV light radiation. Moreover, their flexibility and mechanical stability are maintained after five cycles. To further study their stability for a much longer time, the photocatalytic activity of the samples was examined after 10 months. Figures S12 and S13 showed a slight change in the photodegradation rate, indicating the photocatalysts' stability over a prolonged period.

According to recent studies, self-cleaning characteristics are essential properties in photoactive fabrics and membranes for commercialization [68]. A layer of ZnO NRs/PAN NFs with adsorbed MB was used to examine the photocatalytic self-cleaning ability by immersing it in 20 mL of DI water. Two different experiments were conducted to evaluate this property. The first experiment was performed under UV light irradiation, and the second experiment was carried out without light (in the dark). The photos of the color changes during experiments are exhibited in Fig. S14. The MB absorbed on the membrane was degraded after 210 min under light illumination, and the membrane became colorless, as observed by the naked eye. Additionally, PAN NFs have been utilized in the fabrication of ultrafiltration membranes, wound dressings, and air filtration systems [69]. Therefore, the growth of ZnO NRs with excellent stability and repeatability in photocatalysis can lead to the development of multi-functional materials.

Piezo-photocatalytic performance under UV light irradiation

It is well established that external vibration can bend ZnO NRs and induce a built-in electric field, which enhances charge separation under light illumination [19, 70]. Different studies have reported that a piezoelectric field generates negative piezo potential in the compressive region and positive piezo potential in the tensile strain region [71–73]. Therefore, photo-generated electrons can migrate to the positive piezo-potential surface, and the holes migrate to the negative piezo-potential surface of ZnO. This piezo-potential can facilitate the spatial separation of photoinduced electron–hole pairs on the ZnO NRs' surface and decrease the charge carrier recombination, leading to enhanced photocatalytic performance [71, 72]. To analyze the contribution of the piezoelectric effect to our photocatalysts, the photodegradation process was investigated in an ultrasound bath, which serves as a vibration source to induce piezoelectricity in the ZnO nanorods (ZnO NRs). The photocatalytic degradation of MB under UV illumination was examined under various conditions: dark (without light illumination and ultrasound vibration), US (without light illumination and ultrasound vibration), and US + light (with both light illumination and ultrasound vibration). The results of all these processes are depicted in Fig. 8c. To compare the capability of each sample, Figs. S15–S17 show the plot of ln (C_0/C) as a function of UV light photodegradation of each sample under the same conditions. Accordingly, the corresponding rate constants for the Ag NPs/ZnO NRs/PAN

Table 1 Comparison of apparent rate constant (min^{-1}) under ultrasound vibration (US), light, and simultaneous light + US

Sample	$K_{US} \times 10^{-2}$ (min^{-1})	$K_{Light} \times 10^{-2}$ (min^{-1})	$K_{US+Light} \times 10^{-2}$ (min^{-1})
Ag NPs/ZnO NRs/PAN NFs	0.26 ± 0.01	1.80 ± 0.05	3.90 ± 0.23
ZnO NRs/PAN NFs	0.15 ± 0.07	0.85 ± 0.05	1.81 ± 0.13
PAN NFs	0.25 ± 0.01	0.26 ± 0.01	0.27 ± 0.01

NFs, ZnO NRs/PAN NFs, and PAN NFs are summarized in Table 1. For better comparison, the degradation efficiencies of the photocatalysts after 120 and 180 min are illustrated in Fig. 8d.

Regarding the results in Table 1, it is worth noting that without a photocatalyst, ultrasound and UV light irradiation alone could not cause significant changes in dye concentration, indicating that the MB molecules could not be directly decomposed by ultrasound or UV light irradiation. Furthermore, PAN NFs were unable to decompose the dye molecules under ultrasound or UV light irradiation, and only adsorption of the dye molecules occurred.

The MB dye is considerably decomposed over the Ag NPs/ZnO NRs/PAN NFs and ZnO NRs/PAN NFs during the 120- and 180-min periods, respectively. Their measured corresponding k values show a two-fold enhancement under US + light conditions compared to light illumination only. Therefore, it implies the role of ultrasonication in inducing piezo-photocatalysis, leading to a higher rate of MB photodegradation. Figure 8e illustrates a possible pathway for piezo-photocatalysis and ROS generation. Upon light illumination on ZnO NRs, the electrons (e^-) can transfer to the conduction band (CB), leaving an equal number of holes in the valence band (VB). The piezoelectric potential, generated by vibration energy in ZnO nanorods (NRs), facilitates the separation of photogenerated electrons and holes, resulting in higher photocatalytic activity.

To compare the obtained results with similar recently published works, Table 2 summarizes piezo-photocatalysts that have been reported for the photodegradation of different organic pollutants. It shows the effectiveness of the Ag NPs/ZnO NRs/PAN NFs in the piezo-photocatalytic process. In comparison to recently reported photocatalytic systems with similar, our Ag NPs/ZnO NRs/PAN nanofibrous mat demonstrates competitive or superior degradation efficiency under mild and scalable conditions. Notably, our material achieves effective dye degradation using a simple and low-temperature synthesis route without the need for toxic reagents or complex setups, making it more suitable for real-world applications. Also, PAN electrospun nanofibers are currently purchased at an industrial scale [74], which promises our sample for future research in real wastewater applications. Moreover, these nanofibers exhibit excellent stability, reusability, self-cleaning, and accessible recovery properties. 82% degradation of methylene blue under natural sunlight is another proof of the practicality of our sample.

Table 2 Comparison of the photocatalytic performance of variously reported piezophotocatalysts with the present Ag NPs/ZnO NRs/PAN nanofiber mat, including experimental conditions and degradation rate constants

Piezophotocatalyst	Ultrasonic source	Initial dye concentration (μM)	Reaction system	Rate constant (k)	Ref
$BaTiO_3$ nanofibers	40 kHz	15.7	50 mg/50 Ml RhB	7.4×10^{-2} min^{-1}	[75]
ZnO/CdS nanofibers	150 W	43.8	25 mg/50 mL Bisphenol A	1.557×10^{-1} min^{-1}	[76]
Ag_3PO_4/ZnO nanowires/ stainless steel mesh	40 kHz, 50 W	31.3	3.0×3.0 cm, ~30 mg/50 mL MB	1.3413×10^{-1} min^{-1}	[77]
Zinc oxide nanorods	40 kHz, 150 W	28.5	20 mg/50 mL AO7	1.726×10^{-2} min^{-1}	[18]
g-C_3N_4/Ag/ZnO	40 kHz, 80 W	20.9	25 mg/50 mL RhB	2.1×10^{-2} min^{-1}	[78]
ZnO-MoS_2	40 kHz, 80 W	15.3	20 mg/60 mL MO	84% in 180 min	[79]
Pd/ZnO nanorod/Ceramic tile	40 kHz, 360 W	10	2.5×2.5 cm /30 mL MO	75% in 30 min	[80]
ZnO nanorods/TiO_2 nanocomposite film	40 kHz, 80 W	15.6	1.5×1.5 cm/50 mL MB	5.2×10^{-2} min^{-1}	[81]
Ag/Al doped ZnO	1000 rpm stirring	20	25 mg/50 mL MO	4.3×10^{-2} min^{-1}	[82]
ZnO NRs/PAN NFs	38 kHz, 230 W	10	1.5 × 4.5 cm^2 /15 mL MB	1.81×10^{-2} min^{-1}	This work
Ag Nps/ZnO NRs/PAN NFs	38 kHz, 230 W	10	1.5 × 4.5 cm^2 /15 mL MB	3.9×10^{-2} min^{-1}	This work

Conclusions

In this study, a ternary Ag NPs/ZnO NRs/PAN NFs photocatalyst was successfully fabricated via electrospinning, chemical bath deposition, and dark reduction, and applied to the degradation of organic dyes and tetracycline under various light sources. The enhanced performance stems from the synergistic plasmonic–semiconductor interaction and piezoelectric-assisted charge separation, which together suppress electron–hole recombination and accelerate pollutant breakdown. Under natural sunlight, the system achieved $82.2 \pm 4.5\%$ MB degradation in 60 min and maintained long-term stability across repeated cycles. Notably, its self-standing architecture eliminates the need for post-treatment separation. Compared to prior studies, this work introduces a scalable, multifunctional platform that combines plasmonic, piezoelectric, and structural advantages—offering a novel and practical solution for advanced wastewater treatment.

Supplementary Information The online version contains supplementary material available at https://doi.org/10.1007/s11164-025-05759-2.

Acknowledgements The authors would like to thank the Research and Technology Council of Sharif University of Technology and Alzahra University for their financial support. A.Z.M. also thanks the Iran National Science Foundation (INSF) for its support through Grant Numbers (4031442 and 4025823).

Author contributions Ghazale Asghari Sarabi: Methodology, Investigation, Data curation, Writing – original draft, Conceptualization. Morasae Samadi: Supervision, Conceptualization, Formal analysis, Validation, Writing – original draft, Writing – review & editing. Habib Bagheri: Writing – review & editing. Md Golam Kibria: Conceptualization, Formal analysis, Writing – review & editing. Alireza Z. Moshfegh: Conceptualization, Formal analysis, Writing – review & editing, Supervision, Funding acquisition.

Data availability Data will be made available on request.

Declarations

Conflict of interest The authors declare that they have no known competing financial interests or personal relationships that could have appeared to influence the work reported in this paper.

References

1. X. Wang, Y. Wang, Z. Zhang, L. Tian, T. Zhu, Y. Zhao, Y. Tong, Y. Yang, P. Sun, Y. Liu, Effect, fate and remediation of pharmaceuticals and personal care products (PPCPs) during anaerobic sludge treatment: a review. Environ. Sci. Technol. **58**, 19095–19114 (2024)
2. J. Yang, S. Shojaei, S. Shojaei, Removal of drug and dye from aqueous solutions by graphene oxide: adsorption studies and chemometrics methods. NPJ Clean Water **5**, 5 (2022)
3. Q. Yi, Z. Li, J. Li, J. Zhou, X. Li, R. Dai, X. Wang, Enhancing oxidants activation by transition metal-modified catalytic membranes for wastewater treatment. Res. Chem. Intermed. **49**, 655–678 (2023)
4. A. Naseri, M. Samadi, M. Ebrahimi, M. Kheirabadi, A.Z. Moshfegh, in *Current Developments in Photocatalysis and Photocatalytic Materials*, ed. by X. Wang, M. Anpo, X. Fu (Elsevier, 2020), pp. 457–473
5. Z. Zheng, S. Tian, Y. Feng, S. Zhao, X. Li, S. Wang, Z. He, Recent advances of photocatalytic coupling technologies for wastewater treatment. Chin. J. Catal. **54**, 88–136 (2023)

6. N. Goodarzi, Z. Ashrafi-Peyman, E. Khani, A.Z. Moshfegh, Recent progress on semiconductor heterogeneous photocatalysts in clean energy production and environmental remediation. Catalysts **13**, 1102 (2023)
7. A. Naseri, M. Samadi, A.Z. Moshfegh, in *UV-Visible Photocatalysis For Clean Energy Production And Pollution Remediation* (2023), pp. 9–26
8. M. Samadi, S. Yousefzadeh, H.S.T. Larijani, K. Rahimi, A. Moshfegh, The superiority of CNT over graphene in $BiVO_4$ nanocomposites for visible light photocatalysis. Opt. Mater. **153**, 115611 (2024)
9. D. Xu, C. Yu, X. Peng, H. Yan, Y. Zhang, Recent advances in carbon quantum dot photocatalysis. Res. Chem. Intermed. **50**, 4597–4617 (2024)
10. Y. Deng, J. Liu, Z. Zhou, L. Li, Y. Shi, R. Tang, W. Li, Y. Huang, Recent advances in piezoelectric coupled with photocatalytic reaction system: synergistic mechanism, enhancement factors, and application. ACS Appl. Mater. Interfaces **16**, 50071–50095 (2024)
11. B. Zhang, M. Zhao, K. Cheng, J. Wu, S. Kubuki, L. Zhang, Y.-C. Yong, Piezoelectric effect coupled advanced oxidation processes for environmental catalysis application. Coord. Chem. Rev. **523**, 216234 (2025)
12. F. Sun, D. Xu, J. Xu, Y. Xie, H. Qi, F. Liu, H. Shao, H. Yu, W. Yu, X. Dong, A self-standing dual-electric field synergistic Janus nanofibre piezoelectric photocatalyst with degradation of antibiotics: performances, DFT calculation and mechanism unveiling. J. Mater. Sci. Technol. **208**, 278–291 (2025)
13. F. Sun, Q. Xu, X. Wang, C. Luo, M. Zhao, Q. Ma, H. Yu, W. Yu, X. Dong, Multi-electric field-enhanced $CuInS_2$-modified TiO_2(Anatase)/TiO_2(Rutile)/PVDF nanofiber membrane for multifunctional piezo-photocatalysis, *Adv. Funct. Mater.* 05795
14. P. Jia, J. Li, H. Huang, Piezocatalysts and piezo-photocatalysts: from material design to diverse applications. Adv. Funct. Mater. **34**, 2407309 (2024)
15. H. Zheng, Y. Wang, J. Liu, J. wang, K. Yan, K. Zhu, Recent advancements in the use of novel piezoelectric materials for piezocatalytic and piezo-photocatalytic applications. Appl. Catal. B Environ. **341**, 123335 (2024)
16. M. Samadi, M. Zirak, A. Naseri, E. Khorashadizade, A.Z. Moshfegh, Recent progress on doped ZnO nanostructures for visible-light photocatalysis. Thin Solid Films **605**, 2–19 (2016)
17. M. Samadi, M. Zirak, A. Naseri, M. Kheirabadi, M. Ebrahimi, A.Z. Moshfegh, Design and tailoring of one-dimensional ZnO nanomaterials for photocatalytic degradation of organic dyes: a review. Res. Chem. Intermed. **45**, 2197–2254 (2019)
18. J. Ma, J. Ren, Y. Jia, Z. Wu, L. Chen, N.O. Haugen, H. Huang, Y. Liu, High efficiency bi-harvesting light/vibration energy using piezoelectric zinc oxide nanorods for dye decomposition. Nano Energy **62**, 376–383 (2019)
19. S. Abubakar, S.T. Tan, J.Y.C. Liew, Z.A. Talib, R. Sivasubramanian, C.A. Vaithilingam, S.S. Indira, W.-C. Oh, R. Siburian, S. Sagadevan, S. Paiman, Controlled growth of semiconducting ZnO nanorods for piezoelectric energy harvesting-based nanogenerators. Nanomaterials **13**, 1025 (2023)
20. C.-L. Tan, F. Zhang, Y.-H. Li, Z.-R. Tang, Y.-J. Xu, Au clusters-based visible light photocatalysis. Res. Chem. Intermed. **47**, 29–50 (2021)
21. S. Mandal, R. Ananthakrishnan, Double effects of interfacial Ag nanoparticles in a ZnO multipod@$Ag@Bi_2S_3$ Z-scheme photocatalytic redox system: concurrent tuning and improving charge-transfer efficiency. Inorg. Chem. **59**, 7681–7699 (2020)
22. F. Jandaghian, A. Ebrahimian Pirbazari, O. Tavakoli, N. Asasian-Kolur, S. Sharifian, Comparison of the performance of Ag-deposited ZnO and TiO_2 nanoparticles in levofloxacin degradation under UV/visible radiation. J. Hazard. Mater. Adv. **9**, 100240 (2023)
23. F. Sun, Q. Xu, H. Liu, D. Xu, X. Wang, C. Luo, T. Wang, H. Yu, W. Yu, X. Dong, Plasmon and N-vacancy synergistically enhanced tubular carbon nitride-based S-scheme heterojunction photocatalyst with one stone five birds function: pathways, DFT calculation and mechanism insight. J. Catal. **440**, 115813 (2024)
24. F. Sun, D. Xu, Y. Xie, F. Liu, W. Wang, H. Shao, Q. Ma, H. Yu, W. Yu, X. Dong, Tri-functional aerogel photocatalyst with an S-scheme heterojunction for the efficient removal of dyes and antibiotic and hydrogen generation. J. Colloid Interface Sci. **628**, 614–626 (2022)
25. S. Sun, M. Li, Y. Xue, H. Yang, Immobilized photocatalysts with varied macroscopical supports of different morphologies: a review. J. Environ. Chem. Eng. **12**, 113636 (2024)
26. X. Jin, C. Feng, C. Creighton, N. Hameed, J. Parameswaranpillai, N.V. Salim, On the structural evolution of textile grade polyacrylonitrile fibers during stabilization and carbonization: towards the manufacture of low-cost carbon fiber. Polym. Degrad. Stabil. **186**, 109536 (2021)

27. C. Huang, X. Xu, J. Fu, D.-G. Yu, Y. Liu, Recent progress in electrospun polyacrylonitrile nanofiber-based wound dressing. Polymers **14**, 3266 (2022)
28. B. Borban, M.B. Gohain, D. Yadav, S. Karki, P.G. Ingole, Nano-electrospun membranes: green solutions for diverse industrial needs. J. Hazard. Mater. Adv. **12**, 100373 (2023)
29. J. Zhu, Z. Gao, Q. Mao, Y. Gao, Y. Li, X. Zhang, Q. Gao, M. Jiang, S. Lee, A.C.T. van Duin, Advances in developing cost-effective carbon fibers by coupling multiscale modeling and experiments: a critical review. Prog. Mater. Sci. **146**, 101329 (2024)
30. Q. Xu, F. Sun, X. Liu, Y. Hu, C. Luo, X. Wang, H. Shao, H. Yu, W. Yu, X. Dong, Upconverting luminescence and surface plasmon resonance synergistically boost photocatalytic activity of LaOCl:Yb^3+, Er^3+/Bi_2MoO_6/Ag nanofiber S-scheme heterojunction photocatalyst for degradation of organic contaminants. J. Alloy. Compd. **1020**, 179363 (2025)
31. F. Sun, H. Qi, Y. Xie, Q. Ma, W. He, D. Xu, G. Wang, W. Yu, T. Wang, X. Dong, Flexible self-supporting bifunctional [TiO_2/C]//[Bi_2WO_6/C] carbon-based Janus nanofiber heterojunction photocatalysts for efficient hydrogen evolution and degradation of organic pollutant. J. Alloy. Compd. **830**, 154673 (2020)
32. M. Samadi, A.Z. Moshfegh, Recent developments of electrospinning-based photocatalysts in degradation of organic pollutants: principles and strategies. ACS Omega **7**, 45867–45881 (2022)
33. F.F.A. Aziz, S.N. Timmiati, A.A. Jalil, N.A. Rusdan, N.H.R. Annuar, L.P. Teh, Recent innovation on heterogeneous ZnO-based catalysts for enhanced CO_2 hydrogenation. J. Environ. Chem. Eng. **12**, 112976 (2024)
34. D. Sao, S. Pramanik, R. Mandal, B. Panda, S. Mahato, D. Dhak, B. Mukherjee, P.K. Kuiri, R. Nath, Silver nanoparticles assisted structuring of low-dimensional Ag–ZnO nano composites for enhancing photo catalytic properties under solar light. Results Surf. Interfaces **19**, 100485 (2025)
35. B. Li, I.S. Kim, S. Dai, M.N. Sarwar, X. Yang, Heterogeneous Ag@ZnO nanorods decorated on polyacrylonitrile fiber membrane for enhancing the photocatalytic and antibacterial properties. Colloid Interface Sci. Commun. **45**, 100543 (2021)
36. S. Patel, M. Konar, H. Sahoo, G. Hota, Surface functionalization of electrospun PAN nanofibers with ZnO–Ag heterostructure nanoparticles: synthesis and antibacterial study. Nanotechnology **30**, 205704 (2019)
37. A. Baji, V.K. Truong, S. Gangadoo, H. Yin, J. Chapman, M. Abtahi, S.V. Oopath, Durable antibacterial and antifungal hierarchical silver-embedded poly(vinylidene fluoride-co-hexafluoropropylene) fabricated using electrospinning. ACS Appl. Polym. Mater. **3**, 4256–4263 (2021)
38. J. Zhan, W. Zhang, M. Wang, W. Guan, X. Yan, Q. Zhang, H. Wang, Z. Wang, Y. Zhang, L. Zou, Fabrication, characterization and antibacterial properties of ZnO nanoparticles decorated electrospun polyacrylonitrile nanofibers membranes. Mater. Today Commun. **32**, 103958 (2022)
39. B. Danagody, N. Bose, K. Rajappan, Electrospun polyacrylonitrile-based nanofibrous membrane for various biomedical applications. J. Polym. Res. **31**, 119 (2024)
40. L. Zhang, A. Aboagye, A. Kelkar, C. Lai, H. Fong, A review: carbon nanofibers from electrospun polyacrylonitrile and their applications. J. Mater. Sci. **49**, 463–480 (2014)
41. M. Wu, Q. Wang, K. Li, Y. Wu, H. Liu, Optimization of stabilization conditions for electrospun polyacrylonitrile nanofibers. Polym. Degrad. Stab. **97**, 1511–1519 (2012)
42. D.W. Chae, B.C. Kim, Effects of zinc oxide nanoparticles on the physical properties of polyacrylonitrile. J. Appl. Polym. Sci. **99**, 1854–1858 (2006)
43. M. Kardeş, K. Öztürk, A comparative investigation of photocatalyst ZnO nanorods grown on different seed layers: influence of annealing temperature and atmosphere. Res. Chem. Intermed. **50**, 353–372 (2024)
44. M. Liu, G. Lv, L. Tian, T. Liu, X. Yu, X. An, Y. Liu, J. Zhang, Q. Zheng, X. Hou, L. Mei, L. Liao, Synthesis of self-assembled mesoporous ZnO microspheres designed for microwave-assisted photocatalytic degradation of tetracycline. Inorg. Chem. **63**, 20714–20725 (2024)
45. T. Cai, Y. Liu, L. Wang, S. Zhang, J. Ma, W. Dong, Y. Zeng, J. Yuan, C. Liu, S. Luo, "Dark deposition" of Ag nanoparticles on TiO_2: improvement of electron storage capacity to boost "memory catalysis" activity. ACS Appl. Mater. Interfaces **10**, 25350–25359 (2018)
46. M. Kheirabadi, M. Samadi, E. Asadian, Y. Zhou, C. Dong, J. Zhang, A.Z. Moshfegh, Well-designed Ag/ZnO/3D graphene structure for dye removal: adsorption, photocatalysis and physical separation capabilities. J. Colloid Interface Sci. **537**, 66–78 (2019)
47. P. Pujar, D. Gupta, S. Mandal, High-performance low voltage operation of indium zinc tin oxide thin film transistors using chemically derived sodium β-alumina dielectric. J. Mater. Sci. Mater. Electron. **30**, 9097–9105 (2019)

48. M.W. Abebe, A.F. Baye, H. Kim, Poly (acrylic acid)/polysaccharides IPN derived metal free catalyst for rapid hydrogen generation via $NaBH_4$ methanolysis. Int. J. Hydrogen Energy **47**, 32060–32070 (2022)
49. Y.-C. Chang, J.-Y. Guo, Double-sided plasmonic silver nanoparticles decorated copper oxide/zinc oxide heterostructured nanomaces with improving photocatalytic performance. J. Photochem. Photobiol. A Chem. **378**, 184–191 (2019)
50. N. Rosman, W.N. Wan Salleh, F. Aziz, A.F. Ismail, Z. Harun, S.S. Bahri, K. Nagai, Electrospun nanofibers embedding $ZnO/Ag_2CO_3/Ag_2O$ heterojunction photocatalyst with enhanced photocatalytic activity. Catalysts **9**, 565 (2019)
51. T. Sharma, M. Garg, Optical and morphological characterization of ZnO nano-sized powder synthesized using single step sol-gel technique. Opt. Mater. **132**, 112794 (2022)
52. A. Samriti, S. Pujara, T. Thakur, R. Palai, H.C. Gupta, A. Swart, A. Kuznetsov, J. Prakash, Insight into the sunlight-driven photocatalytic activity of ZnO and ZnO/Ag hybrid nanostructures. Next Mater. **8**, 100733 (2025)
53. L. Buengkitcharoen, S. Amnuaypanich, S. Naknonhan, S. Loiha, N. Patdhanagul, A. Makdee, S. Amnuaypanich, Facile synthesis of robust Ag/ZnO composites by sol–gel autocombustion and ion-impregnation for the photocatalytic degradation of sucrose. Sci. Rep. **13**, 12173 (2023)
54. V. Fauzia, A. Yudiana, Y. Yulizar, M.A. Dwiputra, L. Roza, I. Soegihartono, The impact of the Au/Ag ratio on the photocatalytic activity of bimetallic alloy AuAg nanoparticle-decorated ZnO nanorods under UV irradiation. J. Phys. Chem. Solids **154**, 110038 (2021)
55. J. Singh, K. Sahu, R. Singh, T. Som, R.K. Kotnala, S. Mohapatra, Thermal annealing induced strong photoluminescence enhancement in $Ag\text{-}TiO_2$ plasmonic nanocomposite thin films. J. Alloys Compd. **786**, 750–757 (2019)
56. A. Hassan, M.F. Iqbal, S. Maksym, M. Tetiana, M. Azam, Z. Kanwal, I. Irfan, B Li, Y. Jiang, Near-band-edge emission enhancement and suppression of the deep levels in Ga-doped ZnO via surface plasmon-exciton coupling without a dielectric spacer. J. Mater. Sci. Mater. Electron. **30**, 20544–20550 (2019)
57. X. Wang, Q. Ye, L.-H. Bai, X. Su, T.-T. Wang, T.-W. Peng, X.-Q. Zhai, Y. Huo, H. Wu, C. Liu, Y.-Y. Bu, X.-H. Ma, Y. Hao, J.-P. Ao, Enhanced UV emission from ZnO on silver nanoparticle arrays by the surface plasmon resonance effect. Nanoscale Res. Lett. **16**, 8 (2021)
58. X. Yang, H. Yu, X. Guo, Q. Ding, T. Pullerits, R. Wang, G. Zhang, W. Liang, M. Sun, Plasmon-exciton coupling of monolayer MoS_2-Ag nanoparticles hybrids for surface catalytic reaction. Mater. Today Energy. **5**, 72–78 (2017)
59. M. Faraji, M. Yousefi, S. Yousefzadeh, M. Zirak, N. Naseri, T.H. Jeon, W. Choi, A.Z. Moshfegh, Two-dimensional materials in semiconductor photoelectrocatalytic systems for water splitting. Energ. Environ. Sci. **12**, 59–95 (2019)
60. M. Zirak, M. Ebrahimi, M. Zhao, O. Moradlou, M. Samadi, A. Bayat, H.L. Zhang, A.Z. Moshfegh, Fabrication and surface stochastic analysis of enhanced photoelectrochemical activity of a tuneable MoS2–CdS thin film heterojunction. RSC Adv. **6**, 16711–16719 (2016)
61. M. Zou, C. Tan, H. Yang, D. Kuang, Z. Nie, H. Zhou, Facile preparation of recyclable and flexible $BiOBr@TiO_2$/PU-SF composite porous membrane for efficient photocatalytic degradation of mineral flotation wastewater. J. Water Process Eng. **50**, 103127 (2022)
62. M. Zou, C. Tan, Y. Zhang, J. Hu, Z. Ma, Z. Yuan, L. Zhang, M. Wu, H. Zhou, Exploring the potential of flexible CdS/ZnO/Polyurethane nanocomposite membrane for wastewater remediation. J. Environ. Chem. Eng. **11**, 110135 (2023)
63. M. Zou, C. Tan, X. Liu, Z. Yuan, W. Liu, L. Zhang, X. Yan, X. Zhao, H. Zhou, Ultrafast photosensitized degradation of xanthates by using methylene blue as photosensitizer under simulated and natural solar light irradiation: operational parameters, mechanism and toxicity evolution. J. Water Process Eng. **60**, 105200 (2024)
64. J.-C. Sin, S.-M. Lam, H. Zeng, H. Lin, H. Li, L. Huang, S.-J. Liaw, A.R. Mohamed, J.-W. Lim, K. Dong, Z. Qin, Design and synthesis of Fe_2WO_6/Eu-doped BiOBr nanocomposite: a novel 0D/2D Z-scheme heterojunction system for simultaneous boosted visible-light driven photocatalytic bisphenol A degradation and Cr(VI) reduction. Ceram. Int. **50**, 5372–5383 (2024)
65. H. Zeng, J.-C. Sin, S.-M. Lam, H. Li, H. Lin, L. Huang, H. Huang, L. Xu, K. Dong, C.-K. Goy, A.R. Mohamed, J.-W. Lim, Integration of $SnFe_2O_4$ nanoparticles onto BiOBr nanosheets to form a new 0D/2D Z-scheme nanocomposite for ameliorating synchronous visible light photocatalytic eradication of organic pollutants and Cr(VI) in wastewater. Surf. Interfaces **67**, 106614 (2025)

66. S.-M. Lam, Z.-J. Yong, J.-C. Sin, A.R. Mohamed, H. Zeng, H. Li, H. Lin, L. Huang, H. Huang, L. Xu, J.-W. Lim, K. Dong, Improved photoelectrochemical activity of $NiFe_2O_4/Bi_2WO_6$ photoanode by ZnO nanorod array layer for bifunctional photocatalytic fuel cell. Appl. Surf. Sci. **691**, 162702 (2025)
67. K.-L. Lim, J.-C. Sin, S.-M. Lam, H. Zeng, H. Lin, H. Li, L. Huang, A.R. Mohamed, J.-W. Lim, Integration of Bi_2WO_6 nanoparticles onto $SrTiO_3$ microflowers for efficient solar light-driven photocatalytic cefixime degradation and hexavalent chromium reduction. Inorg. Chem. Commun. **174**, 114063 (2025)
68. Y. Zhang, Q. Li, Q. Gao, S. Wan, P. Yao, X. Zhu, Preparation of Ag/β-cyclodextrin co-doped TiO_2 floating photocatalytic membrane for dynamic adsorption and photoactivity under visible light. Appl. Catal. B Environ. **267**, 118715 (2020)
69. S.K. Nataraj, K.S. Yang, T.M. Aminabhavi, Polyacrylonitrile-based nanofibers: a state-of-the-art review. Prog. Polym. Sci. **37**, 487–513 (2012)
70. V. Consonni, A.M. Lord, Polarity in ZnO nanowires: a critical issue for piezotronic and piezoelectric devices. Nano Energy **83**, 105789 (2021)
71. Y. Wu, D. Yang, Y. Zhang, S. Jiao, W. Tang, Z. Wang, N. Wu, Y. Wang, W. Zhong, A. Zhang, J. Hao, H.-L. Cai, X.S. Wu, Integrated unit-cell-thin MXene and Schottky electric field into piezo-photocatalyst for enhanced photocarrier separation and hydrogen evolution. Chem. Eng. J. **439**, 135640 (2022)
72. G.-C. Lee, L.-M. Lyu, K.-Y. Hsiao, Y.-S. Huang, T.-P. Perng, M.-Y. Lu, L.-J. Chen, Induction of a piezo-potential improves photocatalytic hydrogen production over $ZnO/ZnS/MoS_2$ heterostructures. Nano Energy **93**, 106867 (2022)
73. T. Xian, Y. Zhang, X. Sun, L. Di, C. Sun, W. Jing, H. Wang, H. Yang, S-type Bi_2S_3/BiOBr heterojunction with robust piezo-photocatalytic dye removal activity: degradation performance and mechanism investigation. Opt. Mater. **157**, 116088 (2024)
74. Stellenbosch Nanofiber Company. Polyacrylonitrile (PAN). https://www.sncfibers.com/pan, (accessed August 27, 2025).
75. D. Liu, C. Jin, F. Shan, J. He, F. Wang, Synthesizing $BaTiO_3$ nanostructures to explore morphological influence, kinetics, and mechanism of piezocatalytic dye degradation. ACS Appl. Mater. Interfaces **12**, 17443–17451 (2020)
76. C. Zhang, N. Li, D. Chen, Q. Xu, H. Li, J. He, J. Lu, The ultrasonic-induced-piezoelectric enhanced photocatalytic performance of ZnO/CdS nanofibers for degradation of bisphenol A. J. Alloys Compd. **885**, 160987 (2021)
77. Y. Yu, B. Yao, Y. He, B. Cao, Y. Ren, Q. Sun, Piezo-enhanced photodegradation of organic pollutants on Ag_3PO_4/ZnO nanowires using visible light and ultrasonic. Appl. Surf. Sci. **528**, 146819 (2020)
78. P.P. Gotipamul, S. Abdullah Alqarni, S. Pandiaraj, M. Rathinam, S. Chidambaram, Initiation of piezoelectricity expands the photocatalytic H_2 production and decomposition of organic dye through g-C_3N_4/Ag/ZnO tri-components. Mater. Sci. Energy Technol. **7**, 133–147 (2024)
79. J.A.B. Narvaez, C.C. Mercado, Enhancement of dye degradation in piezo-photocatalytic ZnO–MoS_2 heterostructures. J. Electron. Mater. **53**, 7250–7260 (2024)
80. J. Tian, D. Wang, W. Zheng, H. Zhou, Y. Xiong, H. Zou, S. Ma, C. Han, Y. Huang, Enhanced environmental purification with novel Pd/ZnO nanorod–decorated building materials through piezo-photocatalytic synergistic effect. J. Am. Ceram. Soc. **107**, 3550–3561 (2024)
81. M. Chen, Z. Kang, J. Wu, N. Qin, D. Bao, Significantly enhanced piezo-photocatalytic properties of recyclable nanocomposite films by growing ZnO nanorods on inverse opal structured TiO_2 framework. J. Alloys Compd. **985**, 174032 (2024)
82. I. Changmai, M. Sandilya, S. Deka, B. Choudhury, B.K. Sarma, Exploration of piezo-/pyro-/photocatalytic properties of Ag/AZO nanocomposite and emerging scavenging actions of biomimetic hydroxyapatite. Appl. Surf. Sci. **689**, 162412 (2025)

Authors and Affiliations

Ghazale Asghari Sarabi[1,4] · Morasae Samadi[2] · Habib Bagheri[3] · Md. Golam Kibria[4] · Alireza Z. Moshfegh[1,5]

✉ Morasae Samadi
m.samadi@alzahra.ac.ir

✉ Alireza Z. Moshfegh
moshfegh@sharif.edu

Ghazale Asghari Sarabi
ghazaleasgharisarabi@gmail.com

Habib Bagheri
bagheri@sharif.edu

Md. Golam Kibria
md.kibria@ucalgary.ca

[1] Center for Nanoscience and Nanotechnology, Institute for Convergence Science and Technology, Sharif University of Technology, Tehran 14588-89694, Iran

[2] Department of Physical Chemistry and Nanochemistry, Faculty of Chemistry, Alzahra University, Tehran 19938-93973, Iran

[3] Environmental and Bio–Analytical Laboratories, Department of Chemistry, Sharif University of Technology, Tehran 11155–9516, Iran

[4] Department of Chemical and Petroleum Engineering, University of Calgary, Calgary, AB T2N1N4, Canada

[5] Department of Physics, Sharif University of Technology, Tehran 11155-9161, Iran

Terms and Conditions

Springer Nature journal content, brought to you courtesy of Springer Nature Customer Service Center GmbH ("Springer Nature").

Springer Nature supports a reasonable amount of sharing of research papers by authors, subscribers and authorised users ("Users"), for small-scale personal, non-commercial use provided that all copyright, trade and service marks and other proprietary notices are maintained. By accessing, sharing, receiving or otherwise using the Springer Nature journal content you agree to these terms of use ("Terms"). For these purposes, Springer Nature considers academic use (by researchers and students) to be non-commercial.

These Terms are supplementary and will apply in addition to any applicable website terms and conditions, a relevant site licence or a personal subscription. These Terms will prevail over any conflict or ambiguity with regards to the relevant terms, a site licence or a personal subscription (to the extent of the conflict or ambiguity only). For Creative Commons-licensed articles, the terms of the Creative Commons license used will apply.

We collect and use personal data to provide access to the Springer Nature journal content. We may also use these personal data internally within ResearchGate and Springer Nature and as agreed share it, in an anonymised way, for purposes of tracking, analysis and reporting. We will not otherwise disclose your personal data outside the ResearchGate or the Springer Nature group of companies unless we have your permission as detailed in the Privacy Policy.

While Users may use the Springer Nature journal content for small scale, personal non-commercial use, it is important to note that Users may not:

1. use such content for the purpose of providing other users with access on a regular or large scale basis or as a means to circumvent access control;
2. use such content where to do so would be considered a criminal or statutory offence in any jurisdiction, or gives rise to civil liability, or is otherwise unlawful;
3. falsely or misleadingly imply or suggest endorsement, approval , sponsorship, or association unless explicitly agreed to by Springer Nature in writing;
4. use bots or other automated methods to access the content or redirect messages
5. override any security feature or exclusionary protocol; or
6. share the content in order to create substitute for Springer Nature products or services or a systematic database of Springer Nature journal content.

In line with the restriction against commercial use, Springer Nature does not permit the creation of a product or service that creates revenue, royalties, rent or income from our content or its inclusion as part of a paid for service or for other commercial gain. Springer Nature journal content cannot be used for inter-library loans and librarians may not upload Springer Nature journal content on a large scale into their, or any other, institutional repository.

These terms of use are reviewed regularly and may be amended at any time. Springer Nature is not obligated to publish any information or content on this website and may remove it or features or functionality at our sole discretion, at any time with or without notice. Springer Nature may revoke this licence to you at any time and remove access to any copies of the Springer Nature journal content which have been saved.

To the fullest extent permitted by law, Springer Nature makes no warranties, representations or guarantees to Users, either express or implied with respect to the Springer nature journal content and all parties disclaim and waive any implied warranties or warranties imposed by law, including merchantability or fitness for any particular purpose.

Please note that these rights do not automatically extend to content, data or other material published by Springer Nature that may be licensed from third parties.

If you would like to use or distribute our Springer Nature journal content to a wider audience or on a regular basis or in any other manner not expressly permitted by these Terms, please contact Springer Nature at

onlineservice@springernature.com